Killing the predator: impacts of highest predator mortality on global-ocean ecosystem structure

David Talmy[1] , Eric Carr[1], Harshana Rajakaruna[2], Selina Våge[3], Anne Willem-Omta[4]

[1]University of Tennessee Knoxville, Department of Microbiology, Knoxville, TN

5 [2]Battele Center for Mathematical Medicine, Steve and Cindy Rasmussen Institute for Genomic Medicine, Columbus, OH

[3]The University of Bergen, Department of Biological Sciences, Norway

[4]Case Western Reserve University, Earth, Environmental, and Planetary Sciences

[*]Corresponding author: dtalmy@utk.edu

10 *Correspondence to*: David Talmy (dtalmy@utk.edu)

Abstract. Recent metanalyses suggest that microzooplankton biomass density scales linearly with phytoplankton biomass density, suggesting a simple, general rule may underpin trophic structure in the global ocean. Here, we use a set of highly simplified food-web models, solved within a global general circulation model, to examine the core drivers of linear predator-prey scaling. We examine a parallel food-chain model which assumes 15 microzooplankton grazers feed on distinct size-classes of phytoplankton, and contrast this with a diamond food-web model allowing shared microzooplankton predation on a range of phytoplankton size classes. Within these two contrasting model structures, we also evaluate the impact of fixed vs. density-dependent microzooplankton mortality. We find that the observed relationship between microzooplankton predators and prey can be reproduced with density-dependent mortality on the highest predator, regardless of choices made about plankton food-web 20 structure. Our findings point to the importance of parameterizing mortality of the highest predator for simple food web models to recapitulate trophic structure in the global ocean.

1. Introduction

25 Over the past decades, there has been considerable progress in our understanding of marine planktonic ecosystems. Both satellite and *in situ* observations have helped to elucidate the biogeography, phenology, and structure of these systems. Much of this knowledge has been incorporated in numerical models to make projections and perform sensitivity analyses, in particular pertaining to the impacts of global change (Dutkiewicz et al. 2013; Henson et al. 2021). As a result, marine ecosystem models have become increasingly detailed and complex, with a particular

focus on improving the representation of the rich diversity of plankton. For example, the European Regional Seas Ecosystem Model (ERSEM) contains 10 different plankton functional types and 3 types of bacteria (Butenschön et al. 2016), whereas the current version of the Plankton Type Ocean Model (PlankTOM11) includes 9 plankton functional types, bacteria, and jellyfish (Wright et al. 2021). The Darwin model uses allometric scaling to model dozens of plankton size classes (Ward et al. 2012; Henson et al. 2021)
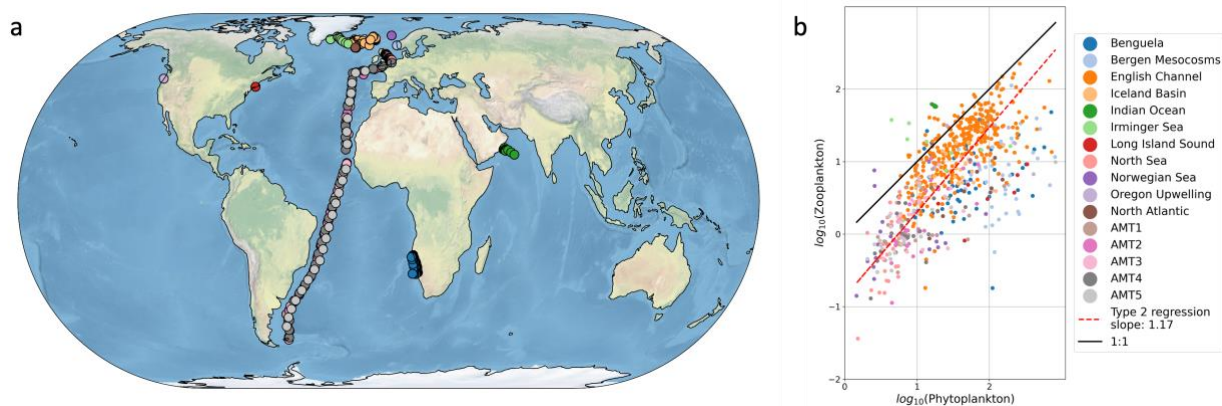
Figure 1. Recent metanalyses suggest microzoopankton biomass density scales linearly with phytoplankton biomass density in the global ocean a) sampling locations and b) relationship between microzooplankton and phytoplankton biomass in mg C m^{-3} (Rajakaruna et al. 2022).

As ecosystem models become increasingly complex, it becomes increasingly challenging to understand how their structure impacts the bulk biogeochemical properties of the system. For example, assumptions about microzooplankton predation on phytoplankton determines model predictions of phytoplankton carbon in the surface ocean, which in turn influences rates of carbon fixation, and eventually, carbon sequestration from the surface layer to the deep ocean. Due to their influence on carbon cycling globally, Earth system models typically contain representations of ocean ecosystems, and are incorporating expanded plankton diversity (Séférian et al. 2020), raising questions about how much model complexity is required to capture biogeochemically relevant properties (Kwiatkowski et al. 2014).

Observational datasets provide a critical resource to discriminate between models with different assumptions about modeled food web interactions (Luo et al. 2022; Petrik et al. 2022). The relationship between microbial predators and prey (for example, microzooplankton and phytoplankton, respectively) is one observed

phenomenon with profound implications for global biogeochemical cycles, for example by controlling the biomass of autotrophs that fix carbon, and impacting carbon export through microzooplankton excretion of fecal pellets (Buck and Newton 1995). One recent metanalysis suggests a relatively simple set of observational relationships between microbial predators and their prey (Rajakaruna et al. 2022). Specifically, predator biomass (say, Y) appears to scale with prey biomass, (say, X), following a simple, linear relationship, i.e. Y~X (Figure 1). These observational compilations present the opportunity to identify key features of ocean biogeochemical models that capture relationships between predator and prey biomass.

Here, we undertake this task with a highly idealized set of ecosystem models, solved in the global ocean with a general circulation model. The models we examine are highly abstracted (Figure 2), capturing some essential features that are general to a wide class of ecosystem and biogeochemical models.

All ecosystem models with descriptions of diversity beyond the classic nutrient-phytoplankton-zooplankton-detritus (NPZD) formulation (Wroblewski 1989; Fasham et al. 1990), must make assumptions about which predators feed on which prey. However, it is unclear whether empirically rooted contrasting assumptions (Holt et al. 1995; Armstrong 1999) about predator preference for prey type impact the scaling between predator and prey biomass, in a manner that is consistent with patterns observed by Rajakaruna et al. (2022). Our models are put forth specifically to address this question.

In addition to asking whether food-web structure impacts plankton predator-prey relationships, we also consider the role of predation on the highest predator, in this case the zooplankton. By their nature, planktonic ecosystem models do not explicitly resolve the dynamics of higher trophic levels. Therefore, the effects of higher predation on the highest predator are usually parameterized (Steele and Henderson 1992; Edwards and Brindley 1999; Rhodes and Martin 2010). The assumptions made here profoundly influence biogeochemical properties such as primary production and chlorophyll distribution (Aumont and Bopp 2006; Stock and Dunne 2010; Yool et al. 2013; Stock et al. 2014; Aumont et al. 2015). However, it is unclear if and how their effects are dependent on choices made about food web structure.

By explicitly examining the role of predation on the highest predator in the context of two contrasting food webs, we seek to identify the core, underlying drivers of linear scaling between microbial predators and prey (Figure 1). We then "sample" the model and compare predictions to observations of trophic structure covering a large range of temperate, subtropical, and tropical ecosystems. In doing so, we evaluate how these contrasting model structures impose trophic structure globally. While our ecosystem models are relatively simple by comparison to many extant biogeochemical models (e.g. Dutkiewicz et al. 2020), they are comparable to the ocean

biology component of many extant Earth system models (Rohr et al. 2023), and allow clear insight. We discuss the implications of our findings for more complex models of ecosystem dynamics.

80

2. Models and Methods

In the sections that follow, we explain and justify the full equations used to parameterize phytoplankton and microzooplankton growth dynamics. We then describe model implementation in a global ocean ecosystem context

85 and the comparison of simulations with a published compilation of relevant ocean data.

2.1 Food-web models

The main ecosystem model parameterization is reported in Table 1, and a schematic representation is provided in

90 Figure 2. Model equations are described in detail in the Appendix, and our source code is provided in a publicly available repository (https://github.com/werdna-spatial/GUD_closure). The most important model parameters are provided in Tables 2 and 3, a more complete list is provided in Table A3, and a fully exhaustive list is provided in the online GitHub repository. We compared predictions of a model with 'diamond food-web' structure (shared predation), to a model assuming predators feed in parallel on distinct prey types:

95

Parallel food-chain model. Here it was assumed that microzooplankton grazers feed in parallel on microzooplankton prey (Armstrong 1999; Ward et al. 2012, 2013), mimicking predation that is specific to different size classes or functional groups. Models with parallel feeding have led to realistic predictions of plankton community composition in the global ocean (Ward et al. 2013; Dutkiewicz et al. 2020). Furthermore, parallel

100 feeding was a component of five of ten Earth system models that were part of the most recent Coupled Model Intercomparison project (CMIP6) evaluated by Rohr et al. (2023), making it a useful food-web structure to examine in a global ocean context.

Diamond food-web model. An alternative to parallel feeding is a model with shared predation. Here,

105 microzooplankton predators may feed on multiple plankton types. Since this general predation resembles a diamond, models with shared predation are referred to as having 'diamond' food-web structure (Holt et al. 1995). A recent study examining plankton community composition along a resource availability gradient in the North

Pacific indicated a model with shared predation on *Prochlorococcus* and heterotrophic bacteria may in some circumstances lead to improved predictions of plankton community composition (Follett et al. 2022). Furthermore,

110 shared predation was a component of six of ten CMIP6 Earth system models evaluated by Rohr et al. (2023), making it a useful model structure to examine in a global ocean context.

Table 1. Plankton ecosystem model equations.

Let the biomass of any plankton size class (either phytoplankton or microzooplankton) be represented generally B_i. Each of these biomass groups is constrained with mass balance equations for advection, mixing, sinking, and biological source and sink terms, as follows:

$$\frac{\partial B_i}{\partial t} = \underbrace{S_{B_i}}_{\substack{Biological \\ reactions}} - \underbrace{\nabla \cdot (\boldsymbol{u}B_i)}_{advection} + \underbrace{\nabla \cdot (\boldsymbol{\kappa}\nabla B_i)}_{diffusion} + \underbrace{\frac{\partial w_i B_i}{\partial z}}_{sinking}$$

Where $\boldsymbol{u}$ and $\boldsymbol{\kappa}$ velocity and diffusion coefficients, respectively, w_i is a sinking speed, and S_{B_i} represents all biological sources and sinks. Let P_i and Z_i represent any phytoplankton and microzooplankton size class, respectively. The planktonic sources and sinks for the diamond food-web and parallel model, respectively, are as follows:

Diamond food-web

$$S_{P_i} = \mu_i P_i - g_i Z_1 - \delta_P P_i$$

$$(1)$$

$$S_{Z_1} = \varepsilon \left(\sum_{i=1,2} g_i \right) Z_1 - \delta_z Z_1 - \delta_{zz} Z_1^2$$

Parallel feeding

$$S_{P_i} = \mu_i P_i - g_i Z_i - \delta_P P_i$$

$$(2)$$

$$S_{Z_i} = \varepsilon g_i Z_i - \delta_z Z_i - \delta_{zz} Z_i^2$$

Where μ_i is the growth rate for each phytoplankton size class, that is sensitive to nutrient availability, light, and temperature. The functional sensitivity of μ_i to these environmental variables, along with mass balances for nutrients and detritus, are described in the Appendix. The grazing rate for each phytoplankton size class is g_i, and the proportion of material ingested into zooplankton biomass is ε. The mortality coefficients for linear and quadratic microzooplankton losses are δ_z and δ_{zz}, respectively.

115 The parallel food chain and diamond food web models use established allometric scaling laws to assign traits according to phytoplankton cell size (Banse 1976; Litchman et al. 2007; Ward et al. 2012; and see Appendix). In both formulations, small and large phytoplankton represent cells with ~0.5 and 7µm equivalent spherical radius, and are representative of picocyanobacteria and eukaryotic algae, respectively. Small and large microzooplankton represent protists with ~3.2 and 4.7µm equivalent spherical radius and are representative of microzooplankton in

120 the ciliate size range. The generalist predator in the diamond food-web model has 3.2µm equivalent cell radius, matching the small predator of the parallel model.

2.2 Parameterizing microzooplankton mortality

125 All lower trophic ecosystem models must make choices about the mortality of the highest predator. Here, loss processes must be mimicked, without being explicitly resolved. This requirement to parameterize presents a problem for plankton ecosystem modelers wishing to motivate model form and function with mechanism. Nevertheless, one way to evaluate the strength of different assumptions about model closure is to examine the influence of contrasting assumptions on the model predictions in a holistic manner. Here, we sought to do this by

130 applying two widely assumed microzooplankton loss processes:

Linear microzooplankton losses. Here, it is assumed that the rate of microzooplankton mortality is independent of its biomass density (Table 1). As such, linear losses may equivalently be thought of as density independent mortality. This assumption has been applied within ecological and biogeochemical models to predict biogeography
135 of cyanobacteria and heterotrophic bacteria in the North Pacific (Follett et al. 2022), and in the global ocean (Ward et al. 2012, 2013).

Quadratic microzooplankton losses. Here, the rate of microzooplankton mortality increases with biomass density. This increase in mortality rate can be justified on several grounds, including intraspecific competition (Barbier and
140 Loreau 2019) and sinking (Schartau et al. 2007), which may both increase with microzooplankton density. Here, we invoke density-dependent mortality on the highest trophic level to mimic the effects of unresolved predation on the highest predator.

Table 2. Size-independent parameters. All parameters were held constant in all simulations, except for the linear
145 and quadratic mortality terms, which were set to zero in simulations where these terms were not considered.

Parameter	Symbol	Value	Units
Linear zooplankton mortality rate	δ_z	0.02	day^{-1}
Quadratic zooplankton mortality rate	δ_{zz}	0.08	m^3 mmol^{-1} day^{-1}
Grazing half-saturation constant	$K_{g,i}$	30	mmol m^{-3}
Grazing assimilation efficiency	ε	0.6	n.d.

Table 3. Size-dependent parameters and scaling coefficients. These were held constant across all simulations.

Parameter	Symbol	a	b	Units
Phytoplankton sinking rate	w	0.06	0.28	m day^{-1}
Maximum phytoplankton growth rate	μ_{max}	2.0,0.6 (large, small)	-0.16	day^{-1}
Ammonium half-saturation constant	$K_{NO_3^-}$	0.17	0.27	mmol m^{-3}
Nitrite half-saturation constant	$K_{NO_2^-}$	0.17	0.27	mmol m^{-3}
Nitrate half-saturation constant	$K_{NH_4^+}$	0.085	0.27	mmol m^{-3}
Phosphorus half-saturation constant	$K_{PO_4^{3-}}$	2.6	0.27	mmol m^{-3}

| Grazer maximum ingestion rate | $g_{max,i}$ | 10 | -0.15 | day^{-1} |

2.3 Global ocean ecosystem models

To explore the ecological and biogeochemical implications of these characteristics, we introduced these parameterizations of primary and secondary producers into a global ocean ecosystem, biogeochemistry, and circulation model (MITgcm). The ecosystem model simulates flow of C, N, and other elements (Figure 2) between inorganic nutrients, photo-autotrophs, microzooplankton, and detritus. It is embedded in a coarse-resolution (1° × 1° horizontal, 24 vertical levels), climatologically averaged, global ocean circulation model that has been constrained with satellite and in situ observations (Wunsch and Heimbach 2007).

2.4 Model-data comparison and statistical analyses

We 'sampled' the model in locations where there are environmental samples in the compilation of Rajakaruna et al. (2022) (Figure 1). After log-transforming phytoplankton and microzooplankton biomass density, we conducted ordinary least squares type 2 (OLS II) regression and quantified a Pearson correlation coefficient. We compared the regression slope and Pearson R value, between the models and the environmental datasets. To identify whether sampling locations were representative of the broader global ecosystem, we repeated the same analysis, sampling the entire global ocean. In doing so, we asked which model assumptions were necessary for the ecosystem model to reproduce internally the observed relationships between microzooplankton and phytoplankton biomass density (Figure 1).

2.5 Sensitivity studies

Our assumed phytoplankton and zooplankton sizes are narrow by comparison to the diversity of plankton sizes that exists in nature, that in some cases is captured by other ecosystem (Ward et al. 2012; Dutkiewicz et al. 2020) and Earth system models (Kearney et al. 2021). To assess the sensitivity of our findings to assumptions about plankton size, we conducted simulations for all four models in which i) the phytoplankton volume was increased by ~3-fold ii) zooplankton volume was increased by ~3-fold % and iii) phytoplankton and zooplankton volumes both were increased by ~3-fold.

Predator feeding assumptions profoundly influence modeled dynamics of phytoplankton and
180   microzooplankton (Rohr et al. 2022). To evaluate the sensitivity of our findings to assumptions about plankton feeding, we conducted simulations in which i) the microzooplankton in the diamond model were allowed to actively switch feeding preference to more abundant prey (see Vallina et al. 2014 and Appendix Equation A21) and ii) microzooplankton preyed upon phytoplankton according to a type III feeding curve (see Rohr et al. 2022 and Appendix Equation A21).

185
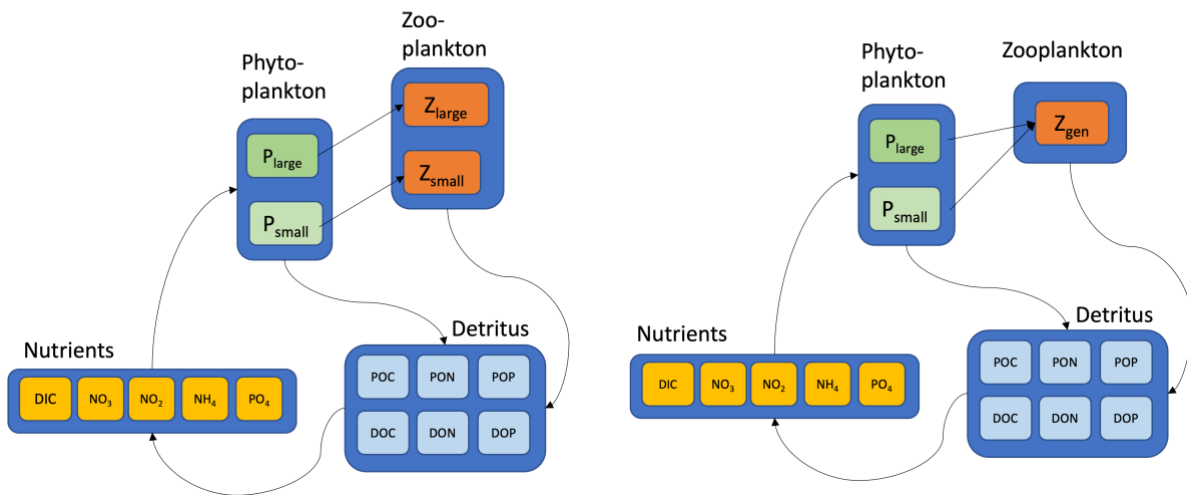
Figure 2: Two contrasting models considered here a) parallel food-chains b) shared predation in the form of a diamond food-web. Both models cycle elements (C, N and P) through inorganic and organic forms. Iron biogeochemistry was included in the model in a manner similar to C, N, and P but is not shown for parsimony. Model equations along with parameter definitions and units are detailed in the Appendix.

3. **Results**

We first describe model predictions of ecosystem structure in the global ocean and go on to examine which of the
190   models leads to predictions of predator and prey biomass density consistent with the observations in Figure 1. In all that follows, we compare the predictions for both the diamond and parallel food chain models with and without density-dependent microzooplankton losses.

3.1 Surface ocean phytoplankton carbon. All models make qualitatively similar predictions of surface ocean total
planktonic carbon (Figure 3). Plankton carbon density is lowest in the low-latitude oligotrophic gyres, and highest
in coastal regions, the equatorial upwelling, and at high latitude. These predictions are all qualitatively consistent
with predictions of phytoplankton biomass density indicated by satellite remote sensing of ocean color (Hu et al.
2019). Interestingly, however, there are clear differences in the total plankton carbon density predicted by the four
models, with the most notable contrast between the models with parallel feeding and the diamond food-web
(compare columns, Figure 3). Specifically, the model with parallel feeding tends to predict greater total
phytoplankton carbon density at high latitude and in equatorial upwelling and coastal regions. There are more subtle
increases in total plankton carbon density when quadratic microzooplankton losses are assumed instead of linear
microzooplankton mortality (compare bottom and top rows in Figure 3). The quadratic closure allows far greater
contribution of phytoplankton to total carbon (Figures S1 and S2), raising total planktonic carbon inventories
globally (Figure 3). Qualitatively similar differences in these four models are found in depth integrated primary
production (Figure S3), carbon export (Figure S4), and secondary production (Figure S5). These results identify a
subtle interplay between food-web structure and microzooplankton mortality on predictions of plankton carbon
density in the global ocean.
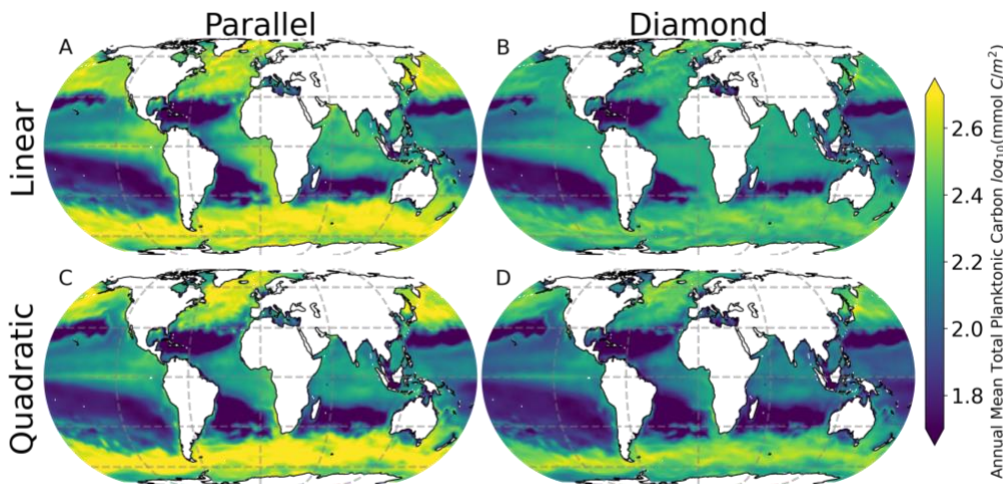
Figure 3. Depth integrated total plankton carbon predicted by all four contrasting models. Color
represents total plankton carbon density averaged over a seasonal cycle.

3.2 Surface Ocean community composition. All four models predict qualitatively similar patterns in phytoplankton community composition in the surface ocean (Figure 4). Specifically, the small phytoplankton size-class dominates in the low-latitude oligotrophic gyres (deep red colors, Figure 4) and the large phytoplankton size class dominates at high latitudes (deep blue colors, Figure 4). Nevertheless, the model with shared predation (diamond food-web)

215 predicts far greater competitive exclusion of the small phytoplankton size-class at high latitude. The parallel food-web model predicts coexistence of the small and large phytoplankton throughout much of the surface ocean, regardless of which microzooplankton closure is used (left-hand column, figure 4).
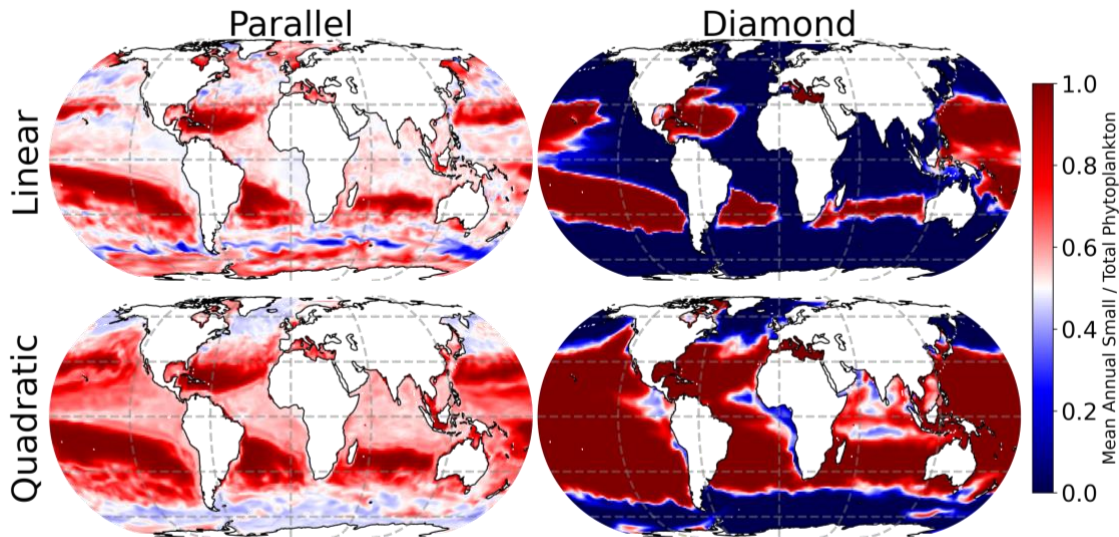
Figure 4. Phytoplankton community composition in the surface ocean. Red indicates dominance
of small phytoplankton; blue indicates dominance of large phytoplankton.

3.3 Interplay between community composition and total carbon density. Interestingly, the impact of food-web

220 structure (diamond vs. parallel) and microzooplankton closure (linear vs. quadratic) appears to be mirrored in the model predictions of plankton carbon density (Figure 3) and community composition (Figure 4). Specifically, the greatest differences are between the diamond and parallel models (comparing columns) with more nuanced differences between closure assumption (comparing rows). This mirroring points to community composition as a driver of total plankton carbon density. Specifically, anywhere in the ocean with greater representation of the

225 smaller size class tends to predict elevated total plankton carbon density.

3.4 Quadratic microzooplankton closure predicts global trophic structure. The results in Figures 3-4 point to the importance of food-web structure for predictions of planktonic ecosystem carbon in the global ocean. We now turn our attention to ask, which of these models is consistent with observations that microzooplankton carbon density scales linearly with phytoplankton carbon density (Figure 1, Rajakaruna et al., 2022).

In Figure 5, we show the relationship between total microzooplankton and phytoplankton carbon for the global ocean. Each colored point represents the number of 1° grid cells falling within the microzooplankton and phytoplankton carbon density marked by its position on the axes. The dashed black line represents the OLS II regression slope. Interestingly, we find here that any differences between the parallel and diamond food-web are minimal (compare columns, Figure 5), and the largest differences are between the linear and quadratic microzooplankton closure (compare rows, Figure 5). Therefore, in predicting ecosystem trophic structure, which we think of here as the relationship between microzooplankton and phytoplankton carbon density, the impacts of food-web on phytoplankton community composition that were revealed in Figures 3-4 cease to play an important role. Moreover, only the model with quadratic microzooplankton losses predicts a relationship between microzooplankton and phytoplankton carbon density that is consistent with the linear scaling in the observation dataset in Figure 1 (bottom row, Figure 5). The model with linear microzooplankton mortality predicts far less correlation between microzooplankton and phytoplankton carbon density (reflected in the lower r values) and a negative slope relating total microzooplankton carbon with phytoplankton carbon.
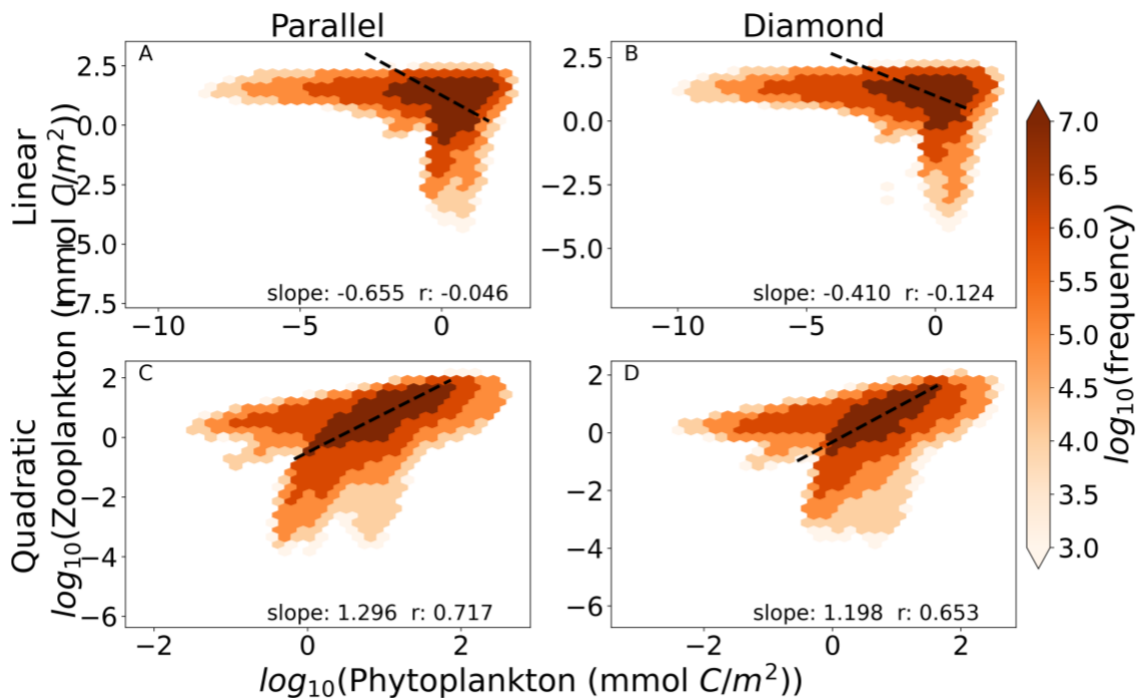
Figure 5: The relationship between phytoplankton and microzooplankton carbon density in the global ocean for a) parallel food chain model with linear closure b) diamond food-web with linear closure c) parallel food chain model with quadratic closure and d) diamond food-web model with quadratic closure. The color within each hexagon represents the number of 1° grid cells that fall within the biomass range marked by their position on the axes. Slopes are OLS Type II regression slopes and r values are Pearson correlation coefficients. Density-dependent microzooplankton mortality reproduces the relationship between Z and P, regardless of food-web structure.

245

Why does the linear closure predict such a variable relationship between microzooplankton and phytoplankton carbon density? To investigate these predictions, we attempted to separate out spatial and temporal impacts on the relationship.

250 In figure 6, we show seasonal variability in the relationship between microzooplankton and phytoplankton carbon density, for a single site in the English Channel. Observations of time-dependent biomass dynamics (Figure 6a) are associated with a strikingly linear relationship between microzooplankton and phytoplankton biomass density (Figure 6b). Consistent with prior analyses (Steele and Henderson 1992; Fasham 1995; Edwards and Brindley

1999; Edwards and Yool 2000) models with linear zooplankton losses predicts oscillations in phytoplankton and microzooplankton biomass (Figure 6c,e), irrespective of whether parallel or diamond food-web structure is assumed. The regression slopes for this single location mirror the regression slopes for the global ocean – the linear microzooplankton closure predicts a shallow regression slope with low r value (Figure 6d,f) and the quadratic closure predicts far higher correlation between phytoplankton and microzooplankton biomass (Figure 6h,j), again consistent with the global collection (Figure 5). Notably, there are many inconsistencies between the modeled time-dependent biomass dynamics and the observations (Figure 6). For example, the quadratic closure predicts a premature spring bloom initiation and termination (Figure 6g,i). Therefore, the correct relationship between phytoplankton and microzooplankton biomass density can be retrieved even when the bloom dynamics are incorrect, pointing to the limitation of biomass scaling relationships as a sole indicator of model performance. Nevertheless, these results demonstrate the tendency of the linear closure to predict predator-prey oscillations as a key driver of the global relationship between phytoplankton and microzooplankton biomass density. The cyclic behavior is true irrespective of assumptions about parallel food-chains vs. a diamond food-web.
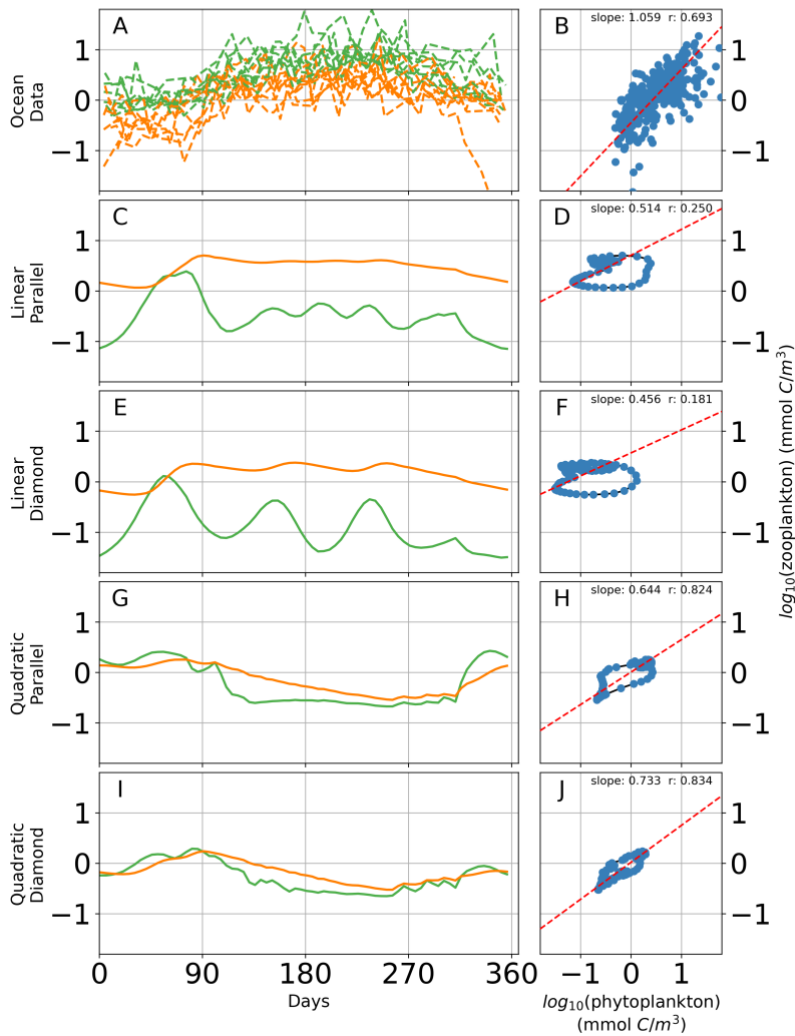
Figure 6: Time dependent biomass dynamics in observational data (a) and across models (c,e,g,i) with corresponding relationships between total microzooplankton and phytoplankton carbon density (d,f,h,j) during a seasonal cycle in the English Channel. Linear losses on the microzooplankton predict cyclic behavior in the predator-prey relationship that are inconsistent with observations (Figure 1).

In Figure 7, we show spatial variation in the Z:P ratio in the surface ocean, where the color in each location represents the seasonally averaged Z:P ratio. Interestingly, there is considerable spatial variability in Z:P for either food-web assuming linear closure (top row, Figure 7), with the Z:P ratio rising at higher latitudes (top row, Figure 7). This prediction is consistent with prior estimates of Z:P variability in the global ocean that assumed linear closure and parallel feeding (Ward et al. 2012). The quadratic closure removes much of this spatial variation (note the narrower color bar range in the bottom row, Figure 7). In steady-state, linear losses on the microzooplankton allows them to place a limit on the phytoplankton biomass, causing carbon to accumulate in the predator (Follett et al. 2022). Density-dependent mortality on the microzooplankton forces the microzooplankton to be removed at a rate that is commensurate with their biomass density, inhibiting their ability to limit the phytoplankton population size, and causing both predators and prey to rise together as the system is enriched with resources.
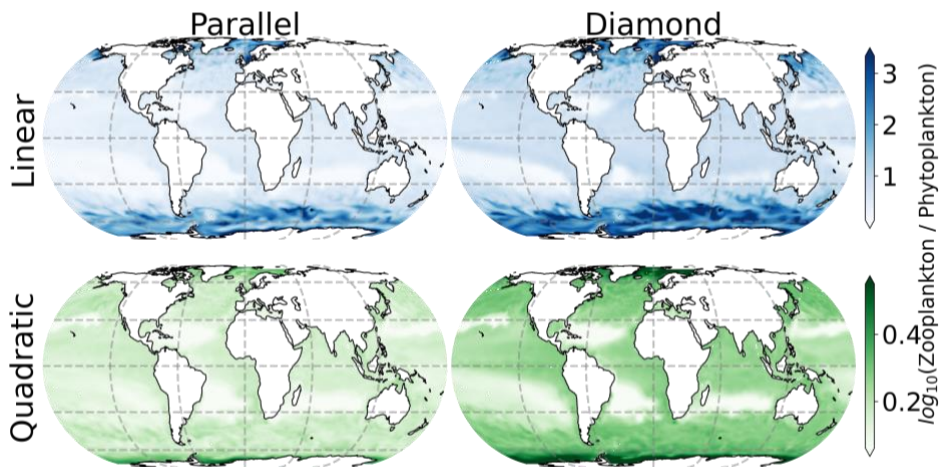
Figure 7. Seasonally averaged surface ocean Z:P ratio. Spatial variability in Z:P ratio is lessened by quadratic microzooplankton losses, irrespective of food-web structure.

Our findings regarding quadratic closure as a driver of linear phytoplankton and microzooplankton biomass scaling are insensitive to different assumption about phytoplankton and microzooplankton size (Figure S6). Furthermore, allowing microzooplankton to switch actively to prey on more abundant phytoplankton allows greater coexistence of phytoplankton in the diamond food web (Figure S7 and Vallina et al. 2014) but unsurprisingly does not

qualitatively modify the scaling relationships reported in Figure 5. Microzooplankton feeding according to type III functional response leads to far greater correlation between predators and prey across models (Figure S8). These results are consistent with prior studies identifying type III feeding as a stabilizing mechanism on microzooplankton-phytoplankton dynamics (Rohr et al., 2022). Nevertheless, even when a type III response is assumed, the quadratic closure still leads to more realistic correlation between microzooplankton and phytoplankton than the linear closure (Figure S8) pointing to the quadratic closure as an important control on trophic structure globally.

4. **Discussion**

Microzooplankton predation on phytoplankton determines phytoplankton carbon in the surface ocean, which in turn influences rates of carbon fixation, and eventually, carbon sequestration from the surface layer to the deep ocean. Models of plankton ecosystem structure are becoming increasingly complex, but models with relatively simple representation of plankton food-webs are important components of many extant Earth system models (Rohr et al. 2023). Here, we have examined a set of models with minimal complexity, in the context of environmental data, to examine core drivers of system structure globally. We find that total phytoplankton carbon density, and community composition, are profoundly impacted by choices regarding food-web structure and losses on the highest predator (in this case, microzooplankton grazers). The diamond food-web predicts competitive exclusion of small and large phytoplankton size-classes, whereas parallel feeding allows the small phytoplankton size class to persist throughout much of the surface ocean, during high latitude blooms and in coastal upwelling regions.

Persistence of small phytoplankton size-classes at higher latitudes is consistent with observational data showing pico (<2µm) and nano plankton (2-20 µm) persist through temperature and resource gradients in a wide range of ocean environments (Marañón et al. 2012). These findings, in tandem with our study and prior modeling studies (Ward et al. 2012, 2013), point to parallel feeding as a pervasive influence on planktonic system structure. Nevertheless, shared predation has been invoked to explain *Prochlorococcus* die-off with latitude (Follett et al. 2022) and is invoked in many extant Earth system models (Rohr et al. 2023). Therefore, both food-web structures considered here (parallel feeding and the diamond food-web) may exist in natural planktonic systems and are also assumed within models of the global ocean that inform climate change projections. Our findings point to the need to carefully consider assumptions about predation on the highest trophic level with application of either model

315 structure, since these have profound implications both for phytoplankton carbon inventories, and community composition.

The food-web model structures assumed here are so simple that they exclude many mechanisms already considered in extant Earth system models. For example, many Earth system models contain representations of both microzooplankton and mesozooplankton. In some cases, these are explicitly represented with multiple state-

320 variables (Stock et al. 2014; Aumont et al. 2015). In others, a single 'adaptive' zooplankton class mimics the effects of micro- and meso-zooplankton by feeding differently on phytoplankton prey types (Moore et al. 2004; Long et al. 2021). Future studies may evaluate the impact of different closures in the context of these more sophisticated structures. Despite the simplicity of our models, we anticipate that our central conclusions will hold in a more general setting. Specifically, assumptions made about highest predator mortality constrain biomass scaling

325 relationships regardless of model predictions about community composition within a trophic level.

By comparison to the models considered here, plankton communities are considerably more complex and diverse, regarding organism size (Hansen et al. 1994), metabolism (Alexander et al. 2015; Posfai et al. 2017) and resource affinities (Litchman et al. 2007). Similarly, when it comes to parameterizing microzooplankton losses, there are more complex assumptions to be made beyond our very crude contrast between linear (density-

330 independent) and quadratic (density-dependent) mortality, again with implications for system properties (Rhodes and Martin 2010; Omta et al. 2023). Despite these limitations, our modeling points to a simple set of principles that we anticipate will extend to more sophisticated representations of plankton ecology. In particular, the quadratic microzooplankton closure provides a realistic and important constraint on the relationship between microzooplankton and phytoplankton carbon density, irrespective of the assumed food-web. This generality and

335 consistency with observational data may also apply to other predator-prey interactions. Linear scaling between predators and prey abundance has also been observed between viruses and heterotrophic bacteria (Rajakaruna et al. 2022). Viral infection is thought to be highly host-specific (Flores et al. 2011) suggesting parallel food-web structure between predators and prey may be more appropriate. Our finding that linear scaling between predators and prey can be reproduced with the quadratic closure, regardless of food-web structure, provides insight that may

340 inform models of plankton ecosystems that include even more diverse representations of microbial life.

Appendix A: Model description.

Here we provide details of the ecosystem model represented graphically in Figure 2. The description is very similar

345 to other implementations of the Darwin ecosystem model (Dutkiewicz et al. 2009, 2012; Ward et al. 2012; Zakem

et al. 2018). All model parameter variable definitions and units are provided in Tables 1 and 2 of the main text, and Tables A1-A3 of this Appendix. An exhaustive list of all parameter values can be found in the online code repository (https://github.com/werdna-spatial/GUD_closure).

Dissolved organic and inorganic material are all governed by a mass balance for advection, diffusion, and biological sources and sinks:

$$\frac{\partial X}{\partial t} = \underbrace{S_X}_{\substack{Biological \\ reactions}} - \underbrace{\nabla \cdot (\boldsymbol{u}X)}_{advection} + \underbrace{\nabla \cdot (\boldsymbol{\kappa}\nabla X)}_{diffusion}$$

(A1)

Where X represents ammonium, nitrate, nitrite, phosphorus, dissolved inorganic carbon (DIC) and iron, as well as pools of dissolved organic carbon, nitrogen, phosphorus, and iron. Pools of particulate detritus follow a similar mass balance but are also assumed to sink at rate w_Y:

$$\frac{\partial Y}{\partial t} = S_{PY} - \nabla \cdot (\boldsymbol{u}Y) + \nabla \cdot (\boldsymbol{\kappa}Y) - \frac{\partial w_Y Y}{\partial z}$$

(A2)

where Y represents carbon, nitrogen, phosphorus, and iron, respectively.

Several of the biological source and sink terms are described in the main text (Table 1). Here we describe additional source and sink terms for inorganic nutrients and detritus. Ammonium is produced by remineralization of organic material, and lost by nitrification and phytoplankton growth:

$$S_{NH_4^+} = \underbrace{r_{DON}DON + r_{PON}PON}_{remineralization} - \underbrace{\zeta_{NH_4^+}NH_4^+}_{nitrification} - \underbrace{\sum_j V_{NH_4^+}P_j}_{nutrient\ uptake}$$

(A3)

Biological source and sink terms for nitrate, nitrite, phosphorus, and dissolved inorganic carbon are as follows:

$$S_{NO_3^-} = \underbrace{\zeta_{NO_2^-}NO_2^-}_{nitrification} - \underbrace{Q_{N:C}\sum_j V_{NO_3^-,j}P_j}_{nitrate\ uptake}$$

(A4)

$$S_{NO_2^-} = \underbrace{\zeta_{NH_4^+}NH_4^+}_{nitrification} - \underbrace{\zeta_{NO_2^-}NO_2^-}_{nitrification} - \underbrace{Q_{N:C}\sum_j V_{NO_2^-,j}P_j}_{nitrite\ uptake}$$

(A5)

$$S_{PO_4^{3-}} = \underbrace{r_{DOP}DOP + r_{POP}POP}_{remineralization} - \underbrace{Q_{P:C} \sum_j V_{DIC,j}P_j}_{phosphate\ uptake} \tag{A6}$$

$$S_{DIC} = \underbrace{r_{DOC}DOC + r_{POC}POC}_{remineralization} - \underbrace{\sum_j V_{DIC,j}P_j}_{DIC\ uptake} \tag{A7}$$

$$S_{Fe} = \underbrace{r_{DOFe}DOFe + r_{POFe}POFe}_{remineralization} - \underbrace{Q_{Fe:C} \sum_j V_{DIC,j}P_j}_{iron\ uptake} \tag{A8}$$

365 Where fixed elemental ratios convert carbon uptake to other elements (e.g. multiplication by $Q_{P:C}$ in Equation A6 converts carbon uptake to phosphorus uptake).

Dissolved organic material, for example DOC, is produced through phytoplankton and zooplankton mortality and sloppy feeding, and consumed through remineralization:

$$S_{DOC} = \underbrace{\sum_i (1 - \beta_p^{mort})\, \delta_p P_i}_{phytoplankton\ mortality} + \underbrace{\sum_j (1 - \beta_z^{mort})(\delta_z Z_j + \delta_{zz} Z_j^2)}_{zooplankton\ mortality} \tag{A9}$$

$$+ \underbrace{\sum_i \sum_j (1 - \beta_z^{graz})(1 - \varepsilon)g_i Z_j}_{sloppy\ feeding} - \underbrace{r_{DOC}DOC}_{remineralization}$$

Dissolved nitrogen and phosphorus are governed by the same sources and sinks, converted from carbon with fixed
370 stoichiometric ratios, e.g. for nitrogen $Q_{N:C}$ (units mol N (mol C)$^{-1}$):

$$S_{DON} = Q_{N:C} \underbrace{\sum_i (1 - \beta_p^{mort})\, \delta_p P_i}_{phytoplankton\ mortality} + Q_{N:C} \underbrace{\sum_j (1 - \beta_z^{mort})(\delta_z Z_j + \delta_{zz} Z_j^2)}_{zooplankton\ mortality} \tag{A10}$$

$$+ Q_{N:C} \underbrace{\sum_i \sum_j (1 - \beta_z^{graz})(1 - \varepsilon)g_i Z_j}_{sloppy\ feeding} - \underbrace{r_{DON}DON}_{remineralization}$$

The same basic processes are also biological sources and sinks for particulate organic carbon:

$$S_{POC} = \underbrace{\sum_i \beta_p^{mort}\, \delta_p P_i}_{phytoplankton\ mortality} + \underbrace{\sum_j \beta_z^{mort}(\delta_z Z_j + \delta_{zz} Z_j^2)}_{zooplankton\ mortality} \tag{A11}$$

$$- \underbrace{\sum_i \sum_j \beta_z^{graz}(1 - \varepsilon)g_i Z_j}_{sloppy\ feeding} - \underbrace{r_{POC}POC}_{remineralization}$$

Where β_p^{mort} and β_Z^{mort} partitions phytoplankton and zooplankton losses between particulate and dissolved pools, with corresponding partitions for sloppy feeding given by β_p^{graz} and β_Z^{graz}. As with DOM (Equation A10), fixed stoichiometric conversations are applied to convert carbon POC sources to PON and POP. These equations are not shown for brevity.

The phytoplankton growth rate μ_i is modified by light, nutrients, and temperature in a multiplicative manner:

$$\mu_i = \mu_{max,i}\gamma_{L,i}\gamma_{N,i}\gamma_{T,i} \tag{A12}$$

Where light limitation is based on the model of photoacclimation following Geider et al. (1997):

$$\gamma_{L,i} = \left(1 - \exp\left(\frac{-\alpha\theta I}{\mu_{max,i}\gamma_{N,i}\gamma_{T,i}}\right)\right) \tag{A13}$$

Nutrient limitation follows Monod kinetics and Liebig's law of the minimum:

$$\gamma_N = min\{V_{N,i}, V_{P,i}, V_{Fe,i}\} \tag{A14}$$

Where nutrient limitation by nitrogen, phosphorus, and iron are governed by monod kinetics:

$$V_{N,i} = \frac{NO_3^-}{NO_3^- + K_{NO_3^-}}e^{\Psi NH_4^+} + \frac{NO_2^-}{NO_2^- + K_{NO_2^-}}e^{\Psi NH_4^+} + \frac{NH_4^+}{NH_4^+ + K_{NH_4^+}} \tag{A15}$$

$$V_{P,i} = \frac{PO_4^{3-}}{PO_4^{3-} + K_{PO_4^{3-}}} \tag{A16}$$

$$V_{Fe,i} = \frac{Fe}{Fe + K_{Fe}} \tag{A17}$$

Where nitrate and nitrite assimilation are inhibited in the presence of ammonium with Ψ, following (Follows et al. 2007) and others l (Dutkiewicz et al. 2009, 2012; Ward et al. 2012; Zakem et al. 2018). Uptake of ammonium, nitrite, and nitrate are found by partitioning total realized nutrient uptake by the three different nitrogen species as follows:

$$V_{NH_4^+,i} = \frac{1}{V_{N,i}}\frac{NH_4^+}{NH_4^+ + K_{NH_4^+}}\gamma_N \tag{A18}$$

$$V_{NO_2^-,i} = \frac{1}{V_{N,i}} \frac{NO_2^-}{NO_2^- + K_{NO_2^-}} e^{\Psi NH_4^+} \gamma_N \tag{A19}$$

$$V_{NO_3^-,i} = \frac{1}{V_{N,i}} \frac{NO_3^-}{NO_3^- + K_{NO_3^-}} e^{\Psi NH_4^+} \gamma_N \tag{A32}$$

Growth is modulated by temperature with the Arrhenius equation:

$$\gamma_T = \tau \exp\left(A_E \left(\frac{1}{T + 273.15} - \frac{1}{T_0} \right) \right) \tag{A20}$$

390 Grazing rate of zooplankton type j follows a Type II or III functional response as a function of total phytoplankton biomass (Holling 1959), partitioned between phytoplankton size classes according to the proportion of total phytoplankton biomass in each size class:

$$g_{i,j} = g_{max,j} \frac{P_i^\beta}{\sum_i P_i^\beta} \frac{(\sum_i P_i)^\gamma}{(\sum_i P_i)^\gamma + K_{g,j}^\gamma} \tag{A21}$$

Here, the value of β switching the grazers from passive ($\beta = 1$) to active ($\beta = 2$) switching and the value of γ switching from a Type II ($\gamma = 2$) to a Type III ($\gamma = 3$) functional response (Vallina et al. 2014). Our main
395 simulations assumed passive switching and Type II functional response, but we conducted sensitivities to both assumptions, separately allowing active prey switching and Type III functional response.

Table A1. Model state variables.

Symbol	Description	Units
NH_4^+	Ammonium	mmol m^{-3}
NO_3^-	Nitrate	mmol m^{-3}
NO_2^-	Nitrite	mmol m^{-3}
PO_4^{3-}	Phosphate	mmol m^{-3}
DIC	Dissolved inorganic carbon	mmol m^{-3}
Fe	Iron	mmol m^{-3}
DOC	Dissolved organic carbon	mmol m^{-3}
DON	Dissolved organic nitrogen	mmol m^{-3}
DOP	Dissolved organic phosphorus	mmol m^{-3}
$DOFe$	Dissolved organic iron	mmol m^{-3}
POC	Particulate organic carbon	mmol m^{-3}
PON	Particulate organic nitrogen	mmol m^{-3}
POP	Particulate organic phosphorus	mmol m^{-3}
$POFe$	Particulate organic iron	mmol m^{-3}

Table A2. Biological source and sink variables.

Symbol	Description	Units
$S_{NH_4^+}$	Biological sources and sinks of ammonium	mmol m^{-3} s^{-1}
$S_{NO_3^-}$	Biological sources and sinks of nitrate	mmol m^{-3} s^{-1}
$S_{NO_2^-}$	Biological sources and sinks of nitrite	mmol m^{-3} s^{-1} 410
$S_{PO_4^{3-}}$	Biological sources and sinks of phosphate	mmol m^{-3} s^{-1}
S_{DIC}	Biological sources and sinks of DIC	mmol m^{-3} s^{-1}
S_{Fe}	Biological sources and sinks of iron	mmol m^{-3} s^{-1}
S_{DOC}	Biological sources and sinks of DOC	mmol m^{-3} s^{-1} 415
S_{DON}	Biological sources and sinks of DON	mmol m^{-3} s^{-1}
S_{DOP}	Biological sources and sinks of DOP	mmol m^{-3} s^{-1}
S_{DOFe}	Biological sources and sinks of DOFe	mmol m^{-3} s^{-1}
S_{POC}	Biological sources and sinks of POC	mmol m^{-3} s^{-1}
S_{PON}	Biological sources and sinks of PON	mmol m^{-3} s^{-1} 420
S_{POP}	Biological sources and sinks of POP	mmol m^{-3} s^{-1}
S_{POFe}	Biological sources and sinks of POFe	mmol m^{-3} s^{-1}

Table A3. Model parameters and variables. Specific parameter values assume default values listed in various publications (Ward et al. 2012; Dutkiewicz et al. 2020) and are available in our online repository (https://github.com/werdna-spatial/GUD_closure/tree/main/Paper_Data). Plankton traits (nutrient and grazing half-saturation constants, maximal grazing and nutrient uptake rates) were generated via allometric scaling relationships reported by Ward et al. (2012), and a subset of these is reported in Table 3. The large phytoplankton has a faster maximal growth rate and higher nutrient half-saturation constants than the small phytoplankton, representative of differences in growth rate between a eukaryotic algae and a cyanobacteria, respectively (Table 2 and 3; Litchman et al. 2007; Ward et al. 2012).

Symbol	Description	Value and Units
w_{POC}	Particulate organic carbon sinking rate	10 m day^{-1}
w_{PON}	Particulate organic nitrogen sinking rate	10 m day^{-1}
w_{POP}	Particulate organic phosphorus sinking rate	10 m day^{-1}
w_{POFe}	Particulate organic iron sinking rate	10 m day^{-1}
r_{DOC}	Particulate organic carbon remineralization rate	0.033 day^{-1}
r_{DON}	Particulate organic nitrogen remineralization rate	0.033 day^{-1}
r_{DOP}	Particulate organic phosphorus remineralization rate	0.033 day^{-1}
r_{DOFe}	Particulate organic iron remineralization rate	0.033 day^{-1}
r_{POC}	Dissolved organic carbon remineralization rate	0.033 day^{-1}
r_{PON}	Dissolved organic nitrogen remineralization rate	0.033 day^{-1}
r_{POP}	Dissolved organic phosphorus remineralization rate	0.033 day^{-1}
r_{POFe}	Dissolved organic iron remineralization rate	0.033 day^{-1}
$\zeta_{NH_4^+}$	Rate of ammonium oxidation to nitrite	2.0 day^{-1}
$\zeta_{NO_2^-}$	Rate of nitrite oxidation to nitrate	0.1 day^{-1}
$V_{NH_4^+,i}$	Rate of ammonium uptake by phytoplankton i	allometric day^{-1}
$V_{NO_3^-,i}$	Rate of nitrate uptake by phytoplankton i	allometric day^{-1}
$V_{NO_2^-,i}$	Rate of nitrite uptake by phytoplankton i	allometric day^{-1}
$V_{DIC,i}$	Rate of DIC uptake by phytoplankton i	allometric day^{-1}

$Q_{N:C}$	Phytoplankton ratio of nitrogen to carbon	0.13 mol N (mol C)$^{-1}$
$Q_{P:C}$	Phytoplankton ratio of phosphorus to carbon	8.3x10^{-3} mol P (mol C)$^{-1}$
$Q_{Fe:C}$	Phytoplankton ratio of iron to carbon	8.3x10^{-6} mol Fe (mol C)$^{-1}$
β_p^{mort}	Proportion of phytoplankton mortality that goes to POC	0.4,0.1 (large,small) n.d.
β_z^{mort}	Proportion of zooplankton mortality that goes to POC	0.6 n.d.
β_z^{graz}	Proportion of sloppy feeding that goes to POC	0.1 n.d.
δ_p	Phytoplankton linear rate of mortality	0.01 day^{-1}
μ_i	Growth rate of phytoplankton i	variable day^{-1}
$\gamma_{L,i}$	Growth limitation by light	variable n.d.
$\gamma_{N,i}$	Growth limitation by nutrients	variable n.d.
$\gamma_{T,i}$	Growth modulation by temperature	variable n.d.
θ	Phytoplankton chlorophyll to carbon ratio	0.13 mg Chl (mmol C)$^{-1}$
α	Phytoplankton light affinity	1x10^{-6} m^2 mmol C (µmol photons)$^{-1}$ (mg Chl)$^{-1}$
I	Photosynthetically available radiance	variable µmol photons m^{-2} day^{-1}
$\Psi_{NH_4^+}$	Ammonium inhibition of nitrate and nitrite assimilation	4.6 m^3 (mmol N)$^{-1}$
A_E	Temperature response function coefficient	-4000 K
τ	Temperature response function coefficient	0.8 n.d.
T_0	Reference temperature for Arrhenius growth response	293.15 K

435

Acknowledgements

440

DT, HR, and EC were supported by grants from the Simons Foundation, United States (Grant ID: 690671) and the NSF, United States (OCE- 2023680). SV was supported by the Trond Mohn Foundation (Grant ID: TMS2018REK02).

445 ## Data Availability Statement

All observational data are from previously published literature.

Code Availability Statement

450

Code used to generate model results are available in a publicly available online repository: https://github.com/werdna-spatial/GUD_closure

Competing Interests

455

The declare that they have no competing interests.

Autor Contributions

460 DT, SV, AW, and HR were involved in study design, DT and EC performed simulations, DT, EC, and AW performed model-data comparisons. DT, SV, and AW contributed to writing and editing.

References

465 Alexander, H., B. D. Jenkins, T. A. Rynearson, and S. T. Dyhrman. 2015. Metatranscriptome analyses indicate resource partitioning between diatoms in the field. Proc. Natl. Acad. Sci. **112**: E2182–E2190.

Armstrong, R. A. 1999. Stable model structures for representing biogeochemical diversity and size spectra in plankton communities. J. Plankton Res. **21**: 445–464.

Aumont, O., and L. Bopp. 2006. Globalizing results from ocean in situ iron fertilization studies. Global Biogeochem. Cycles **20**: 1–15.

Aumont, O., C. Ethé, A. Tagliabue, L. Bopp, M. Gehlen, C. Ethe, A. Tagliabue, L. Bopp, and M. Gehlen. 2015. PISCES-v2: An ocean biogeochemical model for carbon and ecosystem studies. Geosci. Model Dev. **8**: 2465–2513.

Banse, K. 1976. Rates of growth, respiration and photosynthesis of unicellular algae as related to cell size - a review. J. Phycol. **12**: 135–140.

Barbier, M., and M. Loreau. 2019. Pyramids and cascades: a synthesis of food chain functioning and stability. Ecol. Lett. **22**: 405–419.

Buck, K. R., and J. Newton. 1995. Fecal pellet flux in Dabob Bay during a diatom bloom: Contribution of microzooplankton. Limnol. Oceanogr. **40**: 306–315.

Butenschön, M., J. Clark, J. N. Aldridge, J. Icarus Allen, Y. Artioli, J. Blackford, J. Bruggeman, P. Cazenave, S. Ciavatta, S. Kay, G. Lessin, S. Van Leeuwen, J. Van Der Molen, L. De Mora, L. Polimene, S. Sailley, N. Stephens, and R. Torres. 2016. ERSEM 15.06: A generic model for marine biogeochemistry and the ecosystem dynamics of the lower trophic levels. Geosci. Model Dev. **9**: 1293–1339.

Dutkiewicz, S., P. Cermeno, O. Jahn, M. J. Follows, A. A. Hickman, D. A. A. Taniguchi, and B. A. Ward. 2020. Dimensions of marine phytoplankton diversity. Biogeosciences **17**: 609–634.

Dutkiewicz, S., M. J. Follows, and J. G. Bragg. 2009. Modeling the coupling of ocean ecology and biogeochemistry. Global Biogeochem. Cycles **23**: GB4017.

Dutkiewicz, S., J. R. Scott, and M. J. Follows. 2013. Winners and losers: Ecological and biogeochemical changes in a warming ocean. Global Biogeochem. Cycles **27**: 463–477.

Dutkiewicz, S., B. S. Ward, F. Monteiro, and M. J. Follows. 2012. Interconnection of nitrogen fixers and iron in the Pacific Ocean: Theory and numerical simulations. Global Biogeochem. Cycles **26**: GB1012.

Edwards, A. M., and J. Brindley. 1999. Zooplankton mortality and the dynamical behaviour of plankton population models. Bull. Math. Biol. **61**: 303–339.

Edwards, A. M., and A. Yool. 2000. The role of higher predation in plankton population models. J. Plankton Res. **22**: 1085–1112.

Fasham, M. J. R. 1995. Variations in the seasonal cycle of biological production in subarctic oceans: A model sensitivity analysis. Deep Sea Res. Part I Oceanogr. Res. Pap. **42**: 1111–1149.

Fasham, M. J. R., H. W. Ducklow, and S. M. McKelvie. 1990. A nitrogen-based model of plankton dynamics in the oceanic mixed layer. J. Mar. Res. **48**: 591–639.

500 Flores, C. O., J. R. Meyer, S. Valverde, L. Farr, and J. S. Weitz. 2011. Statistical structure of host-phage interactions. Proc. Natl. Acad. Sci. U. S. A. **108**: 288–297.

Follett, C. L., S. Dutkiewicz, F. Ribalet, E. Zakem, D. Caron, E. . V. Armbrust, and M. J. Follows. 2022. Trophic interactions with heterotrophic bacteria limit the range of *Prochlorococcus*. Proc. Natl. Acad. Sci. U. S. A. **119**: 1–10.

505 Follows, M. J., S. Dutkiewicz, S. Grant, and S. W. Chisholm. 2007. Emergent biogeography of microbial communities in a model ocean. Science (80-.). **315**: 1843–1846.

Geider, R. J., H. L. MacIntyre, and T. M. Kana. 1997. Dynamic model of phytoplankton growth and acclimation: responses of the balanced growth rate and the chlorophyll a: carbon ratio to light, nutrient-limitation and temperature. Mar. Ecol. Prog. Ser. **148**: 187–200.

510 Hansen, B., P. K. Bjornsen, and P. J. Hansen. 1994. The size ratio between planktonic predators and their prey prey size. Limnol. Oceanogr. **39**: 395–403.

Henson, S. A., B. B. Cael, S. R. Allen, and S. Dutkiewicz. 2021. Future phytoplankton diversity in a changing climate. Nat. Commun. **12**: 1–8.

Holling, C. S. 1959. The Components of Predation as Revealed by a Study of Small-Mammal Predation of the
515 European Pine Sawfly. Can. Entomol. **91**: 293–320.

Holt, R. D., J. Grover, and D. Tilman. 1995. Simple rules for interspecific dominance in systems with exploitative and apparent competition. Am. Nat. **144**: 741–771.

Hu, C., L. Feng, Z. Lee, B. A. Franz, S. W. Bailey, P. J. Werdell, and C. W. Proctor. 2019. Improving Satellite Global Chlorophyll a Data Products Through Algorithm Refinement and Data Recovery. J. Geophys. Res.
520 Ocean. **124**: 1524–1543.

Kearney, K. A., S. J. Bograd, E. Drenkard, F. A. Gomez, M. Haltuch, A. J. Hermann, M. G. Jacox, I. C. Kaplan, S. Koenigstein, J. Y. Luo, M. Masi, B. Muhling, M. Pozo Buil, and P. A. Woodworth-Jefcoats. 2021. Using Global-Scale Earth System Models for Regional Fisheries Applications. Front. Mar. Sci. **8**: 1–27.

Kwiatkowski, L., A. Yool, J. I. Allen, T. R. Anderson, R. Barciela, E. T. Buitenhuis, M. Butenschön, C. Enright,
525 P. R. Halloran, C. Le Quéré, L. De Mora, M. F. Racault, B. Sinha, I. J. Totterdell, and P. M. Cox. 2014. IMarNet: An ocean biogeochemistry model intercomparison project within a common physical ocean modelling framework. Biogeosciences **11**: 7291–7304.

Litchman, E., C. A. Klausmeier, O. M. Schofield, and P. G. Falkowski. 2007. The role of functional traits and trade-offs in structuring phytoplankton communities: scaling from cellular to ecosystem level. Ecol. Lett. **10**:
530 1170–1181.

Long, M. C., J. K. Moore, K. Lindsay, M. Levy, S. C. Doney, J. Y. Luo, K. M. Krumhardt, R. T. Letscher, M. Grover, and Z. T. Sylvester. 2021. Simulations With the Marine Biogeochemistry Library (MARBL). J. Adv. Model. Earth Syst. **13**: e2021MS002647.

Luo, J. Y., C. A. Stock, N. Henschke, J. P. Dunne, and T. D. O'Brien. 2022. Global ecological and biogeochemical impacts of pelagic tunicates. Prog. Oceanogr. **205**: 102822.

Marañón, E., P. Cermeño, M. Latasa, and R. D. Tadonléké. 2012. Temperature, resources, and phytoplankton size structure in the ocean. Limnol. Oceanogr. **57**: 1266–1278.

Moore, J. K., S. C. Doney, and K. Lindsay. 2004. Upper ocean ecosystem dynamics and iron cycling in a global three-dimensional model. Global Biogeochem. Cycles **18**: GB4028.

Omta, A. W., E. A. Heiny, H. Rajakaruna, D. Talmy, and M. J. Follows. 2023. Trophic model closure influences ecosystem response to enrichment. Ecol. Modell. **475**: 110183.

Petrik, C. M., J. Y. Luo, R. F. Heneghan, J. D. Everett, C. S. Harrison, and A. J. Richardson. 2022. Assessment and Constraint of Mesozooplankton in CMIP6 Earth System Models. Global Biogeochem. Cycles **36**: 1–25.

Posfai, A., T. Taillefumier, and N. S. Wingreen. 2017. Metabolic Trade-Offs Promote Diversity in a Model Ecosystem. Phys. Rev. Lett. **118**: 1–5.

Rajakaruna, H., A. W. Omta, E. Carr, and D. Talmy. 2022. Linear scaling between microbial predator and prey densities in the global ocean. Environ. Microbiol. **25**: 1–9.

Rhodes, C. J., and A. P. Martin. 2010. The influence of viral infection on a plankton ecosystem undergoing nutrient enrichment. J. Theor. Biol. **265**: 225–237.

Rohr, T., A. J. Richardson, A. Lenton, M. A. Chamberlain, and E. H. Shadwick. 2023. Zooplankton grazing is the largest source of uncertainty for marine carbon cycling in CMIP6 models. Commun. Earth Environ. **4**: 212.

Rohr, T., A. J. Richardson, A. Lenton, and E. Shadwick. 2022. Recommendations for the formulation of grazing in marine biogeochemical and ecosystem models. Prog. Oceanogr. **208**: 102878.

Schartau, M., a. Engel, J. Schröter, S. Thoms, C. Völker, and D. Wolf-Gladrow. 2007. Modelling carbon overconsumption and the formation of extracellular particulate organic carbon. Biogeosciences Discuss. **4**: 13–67.

Séférian, R., S. Berthet, A. Yool, J. Palmiéri, L. Bopp, A. Tagliabue, L. Kwiatkowski, O. Aumont, J. Christian, J. Dunne, M. Gehlen, T. Ilyina, J. G. John, H. Li, M. C. Long, J. Y. Luo, H. Nakano, A. Romanou, J. Schwinger, C. Stock, Y. Santana-Falcón, Y. Takano, J. Tjiputra, H. Tsujino, M. Watanabe, T. Wu, F. Wu, and A. Yamamoto. 2020. Tracking improvement in simulated marine biogeochemistry between CMIP5 and CMIP6. Curr. Clim. Chang. Reports **6**: 95–119.

Steele, J. H., and E. W. Henderson. 1992. The role of predation in plankton models. J. Plankton Res. **14**: 157–172.

Stock, C. A., J. P. Dunne, and J. G. John. 2014. Global-scale carbon and energy flows through the marine planktonic food web: An analysis with a coupled physical-biological model. Prog. Oceanogr. **120**: 1–28.

565 Stock, C., and J. Dunne. 2010. Controls on the ratio of mesozooplankton production to primary production in marine ecosystems. Deep. Res. Part I Oceanogr. Res. Pap. **57**: 95–112.

Vallina, S. M., B. A. Ward, S. Dutkiewicz, and M. J. Follows. 2014. Maximal feeding with active prey-switching: A kill-the-winner functional response and its effect on global diversity and biogeography. Prog. Oceanogr. **120**: 93–109.

570 Ward, B. A., S. Dutkiewicz, and M. J. Follows. 2013. Modelling spatial and temporal patterns in size-structured marine plankton communities: top-down and bottom-up controls. J. Plankton Res. **36**: 31–47.

Ward, B. A., S. Dutkiewicz, O. Jahn, and M. J. Follows. 2012. A size-structured food-web model for the global ocean. Limnol. Oceanogr. **57**: 1877–1891.

Wright, R. M., C. Le Quéré, E. Buitenhuis, S. Pitois, and M. J. Gibbons. 2021. Role of jellyfish in the plankton
575 ecosystem revealed using a global ocean biogeochemical model. Biogeosciences **18**: 1291–1320.

Wroblewski, J. S. 1989. A model of the spring bloom in the North Atlantic and its impact on ocean optics. Limnol. Oceanogr. **34**: 1563–1571.

Wunsch, C., and P. Heimbach. 2007. Practical global oceanic state estimation. Phys. D Nonlinear Phenom. **230**: 197–208.

580 Yool, A., E. E. Popova, and T. R. Anderson. 2013. MEDUSA-2.0: An intermediate complexity biogeochemical model of the marine carbon cycle for climate change and ocean acidification studies. Geosci. Model Dev. **6**: 1767–1811.

Zakem, E. J., A. Al-Haj, M. J. Church, G. L. Van Dijken, S. Dutkiewicz, S. Q. Foster, R. W. Fulweiler, M. M. Mills, and M. J. Follows. 2018. Ecological control of nitrite in the upper ocean. Nat. Commun. ,
585 doi:10.1038/s41467-018-03553-w